Prediction-driven Respiratory Motion Atlas Formation for 4D Image-guided Radiation Therapy in Lung

Xiaoxiao Liu[1], Bradley C. Davis[2], Marc Niethammer[1], Stephen M. Pizer[1], Gig R. Mageras[3]

[1] Department of Computer Science, University of North Carolina at Chapel Hill, NC
[2] Kitware, Inc., Clifton Park, NY
[3] Department of Medical Physics, Memorial Sloan-Kettering Cancer Center, New York, NY

Abstract. Respiratory motion challenges lung radiation therapy with uncertainties of the location of important anatomical structures in the thorax. In order to capture the trajectory of the motion, dense image matching methods and learning-based motion prediction methods have been commonly used. However, both methods have limitations. Serious motion artifacts challenge the intensity-based image matching, and the motion prediction methods require strong motion consistency between the training and test data. This paper proposes a prediction-driven motion atlas framework for motion estimation with artifact-laden images, using a Fréchet-mean-image matching scheme that is softly constrained by deformation predictions. In this framework, all the time-stamped images within a breathing cycle are diffeomorphically deformed to their Fréchet mean. The iterative optimization is driven by both intensity matching forces and prediction matching forces trained from patient-specific planning images. The effectiveness of the framework is demonstrated with computational phantom and real cone-beam CT images.

1 Introduction

Respiratory motion challenges the standard radiation treatment planning procedure in thorax. In fact, positional uncertainties caused by the respiratory motion have been shown to have a large impact on radiation dose [1, 2]. Accurate respiratory motion estimation is necessary for removing the motion-induced uncertainties. In 4D image-guided radiation therapy (IGRT) two different imaging modalities are often used for planning and treatment, respectively. Standard multi-slice respiration-correlated CT (RC-CT) scans are usually taken for diagnosis and planning, for its good contrast and high resolution and large field of view. Immediately prior to treatment, another set of images is acquired for radiation guidance and dose calculation. Factors such as the speed of the scan, the imaging dose and the configuration of the treatment devices determines the feasibility of a certain image modality being adopted at treatment time. Implanted

gold markers and megavoltage (MV) portal imaging are commonly used for setup verification of tumors treated with high-dose, single-fraction radiotherapy.

Cone-beam CT (CBCT) exploits flat panel technology to integrate the imaging system directly into the treatment accelerator, allowing acquisition of a volumetric image at each respiratory phase in the treatment position and eliminating the need for marker implantation [3–5]. However, degradation of image quality (Fig.1) resulting from the sparse projections for each phase in the filtered back-projection reconstructions imposes serious limitations on its IGRT applications [6]. NST technology can provide unprecedented imaging speed and good spatial resolution in the plane perpendicular to the radiation field. However, the resulting images have interfering patterns in comparison to the standard CT scans, making the soft tissue in low contrast

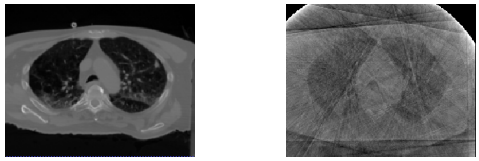

Fig. 1: Left: An axial slice of a diagnostic CT image at the end-inspiration (EI) phase taken at the treatment planning time. Right: An axial slice of a five-minute CBCT scan at EI phase, having significant streak artifacts due to the FBP reconstruction using sparse and unevenly spaced projections.

Motion reduction techniques can increase the contrast-to-noise-ratio (CNR) of the image thus help the image guidance procedure. One of the techniques is to compute an atlas image by averaging all the images after warping onto a common reference image [5]. If the spatial transformation successfully matches the geometries of all the images together, the CT intensity of the anatomical structures will be enhanced in the resulting atlas image. The key is to estimate the correct deformations from the noisy 4D sequence image.

Two different categories of methods have been used to capture the respiratory motion trajectory. One is ordinary intensity-based image matching or tracking. Various non-linear dense image registrations can be used to calculate the spatial changes of each voxel between images by matching their intensity profiles [7, 8]. However, the image registration could easily get trapped in local minima when imaging artifacts are present and thus tends to over-fit to those artifacts.

The other category is linear motion modeling with surrogate signals. Recognizing the hysteresis of respiration, various external and internal surrogate signals have been used for motion modeling and prediction in lung [9–11]. The diaphragm position of the lung has been used as a navigator of the image deformation and used for motion prediction for CBCT-guided radiation therapy [12]. Recently, the shape of the lung has been used as an advanced surrogate for motion prediction, in which the so-called *shape-correlated deformation statistics* (SCDS) reveals the maximum linear correlations between the shape surrogates and the image deformations [13, 14]. The common underlying assumption of all

the surrogate-invovled models is that the correlation between the surrogate deformations and the underlying image deformations is strong and invariant over time (or at least the same between planning time and target time). The assumption simplifies the complicated breathing system and thus enables the estimation by incorporating prior information. However, the correlations between the surrogate and the spatial deformation are often not exactly the same between the planning time and the treatment time, especially for cancer patients who have difficulty in stabilizing their breathing over time. Besides, noise kept in the SCDS trained from few planning phases tend to result in predictions that are not consistent with the actual anatomical conformations in some local regions.

To fully utilize both categories of methods while avoiding their limitations, our method improves the motion estimation by integrating intensity information with motion predictions. On the one hand, the motion prediction can help regularize the intensity matching from over-fitting. On the other hand, meaningful image features can be utilized to reduce prediction errors.

A respiratory motion atlas formation method driven by a combination of prediction matching forces and image matching forces is developed in this paper. A respiratory motion atlas contains an atlas image and the dense image deformations that transform each time-stamped image in the breathing cycle to the atlas image. Instead of an image at an arbitrary time point, a Fréchet mean image that takes the minimum total amount of transformations to match all images is computed and used as the atlas image for increased robustness. The deformations predicted from a shape-correlated deformation statistics (SCDS) model are used as a soft constraint during the optimization. The balancing force between the prediction force and the intensity force can be adjusted via a weighting factor, selected upon the credibility of the training statistics and the quality of the treatment images.

Section 2 introduces the framework of the proposed prediction-driven deformation atlas formation. Specifically, section 2.1 introduces the the background of Fréchet mean image formation; Section 2.2 presents the motion prediction using the SCDS model; Section 2.3 introduces a prediction-driven atlas formation by integrating the predicted deformations into the image matching scheme. Experimental results are presented in Section 3.

2 Methodology

2.1 Respiratory Fréchet mean image formation

To quantify the breathing motion from images, non-linear dense image registrations are often used to compute the spatial changes for each voxel in the image. The breathing motion can be quantified by the non-linear deformations that match each time-stamped image in the breathing cycle to an atlas image. The atlas image, together with the deformations, form the respiratory motion atlas for this patient. There are several aspects to be considered in choosing a proper atlas image. First of all, due to the large anatomical variations between patients,

it is more practical for the atlas image to be patient-specific. Secondly, to be used for motion prediction, the conformation of the atlas image should also be stable over time or at least stable between the planning time and the treatment or target time; Computationally, a smaller total amount of deformations is preferred for better image registration accuracy and efficiency.

A Fréchet mean image has the property that it minimizes the sum of squared distances on the Riemannian manifold of diffeomorphic transformations to a group of images. It represents an averaged spatial configuration of that group [15]. Therefore, the Fréchet mean image of the breathing sequence well satisfies the aforementioned criteria and is used in this paper as the atlas image.

The Fréchet mean formation method based on large deformation diffeomorphic image matching has been successfully applied to regression of longitudinal image data to study non-linear geometric changes and variability of anatomical structures. Note that the Euclidean mean of all the image intensities is inappropriate to represent the geometry of the data that deforms in a non-linear nature. In the process of iteratively updating the Fréchet mean image, the deformations that transform all the phases to the Fréchet mean are optimized at the same time (Fig.2).

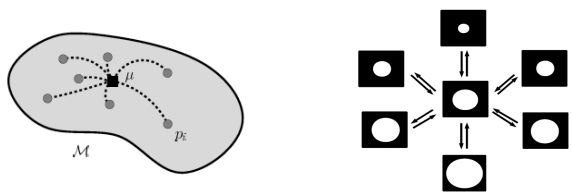

Fig. 2: Fréchet image mechanism: a) The filled circles represent individual point $\mathbf{p}^i$ on the Riemannian manifold $\mathcal{M}$. The Fréchet mean (filled square) is the point μ on the manifold that minimizes the sum of squared distances to the observations. Distances are measured along the manifold; b) Iterative Fréchet mean image construction framework illustrated on images of spheres with varying radius. The mean image in the middle minimizes the sum of squared deformation distances required to match all input images.

Given a group of time-stamped images, geometric changes over time are represented as the action of a group of diffeomorphisms on images. Let $\mathrm{Diff}_V(\Omega)$ be the group of diffeomorphisms that are isotopic to the identity. Each element $\phi : \Omega \to \Omega$ in $\mathrm{Diff}_V(\Omega)$ deforms an image I to the image $I \circ \phi$.

In [15] the geodesic distance between a pair of images on the manifold is defined by diffeomorphic matching:

$$d^2(I^F, I^M) = \mathrm{argmin} \int_0^1 ||v_t||_V^2 dt + \frac{1}{\sigma^2} ||I^M \circ \phi - I^F||_{L2}^2, \tag{1}$$

subject to $\phi(x) = x + \int_0^1 v_t dt$. The first term defines a metric on the space of diffeomorphisms that are generated by integrating velocity fields v. These diffeomorphisms are used to deform a moving image I^M to match a fixed image I^F. The second term penalizes residual image dissimilarity. The parameter σ controls the relative weight of these terms.

The Fréchet mean $\hat{I}$ is the image that requires the least amount of deformation to map onto the group of input images:

$$\hat{I} = \underset{I \in J}{\operatorname{argmin}} \sum_{i=1}^{N} d(I, I^i)^2. \tag{2}$$

Combined with geodesic distance definition (1), the optimization problem can be summarized as

$$\hat{I}, \hat{\phi}^i = \underset{I, \hat{\phi}^i \in \mathbb{I} \times \mathrm{Diff}_V(\Omega)^N}{\operatorname{argmin}} \sum_{1}^{N} \left[\int_0^1 ||v_t^i||_V^2 dt + \frac{1}{\sigma^2} ||I - I^i \circ \phi^i||_{L2}^2 \right],$$
$$\text{subject to } \phi_0^i = Id,\ \phi^i(x) = x + \int_0^1 v_t^i(\phi_t^i(x)) dt. \tag{3}$$

2.2 Deformation prediction using the SCDS model

The SCDS model has been shown to effectively reveal the patient-specific linear correlations between the shape surrogates and the image deformations [13, 14]. In this method, the shape of the lung is used as an internal surrogate signal to navigate the dense image deformation by linear regression. The SCDS model trained from the planning images is used to predict the motion of the target images via extracted shape surrogates. We adopt the SCDS model to calculate the deformation prediction that is going to be used as a soft constraint in the overall optimization framework described in the next section.

In order to apply this method to CBCT images, robustly extracting the lung boundaries against the streak intensity artifacts is important. We developed a posterior probability optimization scheme to calculate the models that fit into the target images while staying in the trained shape space. The optimization is described in

$$\mathbf{log}\ p(\mathbf{q}^i | J^i) = \underset{q^i}{\operatorname{argmax}} [\mathbf{log}\ p(J^i | \mathbf{q}^i) + \mathbf{log}\ p(\mathbf{q}^i)], \tag{4}$$

where $\mathbf{q}^i$ is the lung shape (to distinguish the shapes $\mathbf{p^i}$ in training) of the CBCT image J^i (to distinguish the training image I^i). The image match term or the likelihood term is the summation of a second-order gradient magnitude measured on the surface of the model (see Fig.3), indicating how well the model fits to the boundries. The prior term is measured by Mahalanobis distance of the model in the trained shape space.

In summary, three major steps are carried out to estimate the deformation represented by the dense deformation field $\mathbf{u}^i$ for CBCT image J^i at phase i:

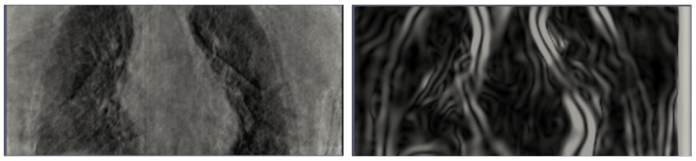

Fig. 3: The second order gradient magnitude image is computed as $||\nabla(||\nabla(G \circ I)||)||$, where G is the gaussian smoothing operator. A coronal slice of an CBCT phase image is shown on the left, with its result shown on the right.

1. The dense image deformations in the planning CTs are obtained by the intensity-based Fréchet mean formation method introduced in the last section. The surface models of the lung are extracted from each CT phase images. Calculated the linear correlation $\mathbf{C}$ that maps a shape surrogate $\mathbf{p}^i$ to its corresponding image deformation $\mathbf{u}^i$, such that $\mathbf{u} = \mathbf{C} \cdot \mathbf{p} + \epsilon$, where ϵ is the regression error.
2. Segment the lung shape $\mathbf{q}^i$ from the CBCT images J^i using the posterior probability optimizaiton scheme.
3. Deformations of each time-point of the CBCT sequence $\mathbf{u}^i$ are calculated by $\mathbf{u}^i = \mathbf{C} \cdot \mathbf{q}^i$.

After the motion prediction, an atlas image can be calculated by averaging all the intensity images after warping them using the predicted deformations.

2.3 Prediction-driven respiratory motion atlas formation

As mentioned in the introduction, when using the proposed SCDS prediction, the correlation between surrogate deformations and underlying image deformations among the training data is assumed to be the same as among the target data. The consistency assumption provides the prerequisite for directly applying the statistics trained from the planning data to the target data. However, the assumption does not hold for lung cancer patients who themselves have difficulties to strictly regularize their breathing patterns. Besides, the linear correlation regression results contain noises due to the small number of sample size.

To increase the prediction robustness of the method, image intensity features can be used to adapt to the motion variations between the training and the testing data. Despite the CBCT artifacts, there are many intensity features useful for guiding the image registration, such as the bony rib cage, and the bronchial structures inside the lung.

A prediction-driven deformation atlas formation method, driven by the combination of prediction constraints and image matching forces is presented here to weaken the consistency assumption and improve the motion estimation accuracy. The deformation predictions are used as soft constraints in the iterative

Fréchet mean image optimization, as follows:

$$\hat{J}, \hat{\varphi}^i = \underset{J,\hat{\varphi^i} \in \mathbb{I} \times \mathrm{Diff}_V(\Omega)^N}{\mathrm{argmin}} \sum_1^N \left[\int_0^1 ||v_t^i||_V^2 dt + \frac{1}{\sigma_1^2} ||J - J^i \circ \varphi^i||_{L2}^2 + \frac{1}{\sigma_2^2} d_R(\varphi^i, \phi^i(q^i)) \right],$$
$$\text{subject to } \varphi^i = x + \int_0^1 v_t^i dt, \tag{5}$$

where J^i denotes the CBCT image at phase i, $\hat{J}$ is the atlas image and φ^i refers to the image deformation that matches the individual CBCT phase image J^i to the atlas image $\hat{J}$, and $\mathbf{q}^i$ is the lung shape segmented from J^i using the deformable segmentation method introduced in Section 2.2. The difference/distance between the varying deformation φ and the prediction $\phi(q^i)$ is measured via the Riemannian manifold metric R, which is defined by

$$d_R(\psi_1, \psi_2) = \underset{\gamma:[0,1]->\mathcal{M}, \gamma(0)=\psi_1, \gamma(1)=\psi_2}{inf} \int_0^1 \sqrt{< \dot{\gamma(t)}, \dot{\gamma(t)} >_V \, dt}, \tag{6}$$

where the Riemannian distance between two points ψ_1 and ψ_2 on $\mathcal{M}$ is defined as the infimum of this integral over all piecewise smooth curves γ that connect ψ_1 and ψ_2. This distance can be alternatively computed by $d_R(\psi_1 \circ \psi_2^{-1}, id)$, where id is the identity transformation.

In order to reduce the computational time and storage, an Euclidean approximation of the Riemannian distance is given by : $d_R(\varphi^i, \phi^i(q^i)) \approx ||\mathbf{u}_{\varphi^i} - \mathbf{u}_{\phi(\mathbf{q}^i)}||_{L^2}^2$, where $\mathbf{u}_\psi$ denotes the dense displacement vector field resulting from the diffeomorphic transformation ψ, and the SCDS-predicted deformation $\mathbf{u}_{\phi^i}(\mathbf{q}^i)$ is computed by linear mapping $\mathbf{u}_{\phi^i}(\mathbf{q}^i) = \mathbf{C} \cdot \mathbf{q}^i$ (refer to Section 2.2). When deformations are not very large, the linear approximation is sufficient.

The balancing force between the prediction and the noisy intensity profile can be adjusted via the weighting factors σ_1 and σ_2, selected upon the credibility of the training statistics and the quality of the treatment images. In general, the weighting factors should make the two forces have the same order of magnitude. Built on top of the original intensity-based atlas formation method (Section.2.1), the new energy term of the prediction is treated as an extra feature channel. Computationally, this extra channel itself is a three-dimensional-vector channel and takes three times the storage as the image intensity.

3 Experimental results

3.1 Breathing spheres

We started with some simulation data to test the prediction-driven atlas formation method. A sequence of sphere images with varying radius were designed to mimic the breathing scenario. The radii follow a sinusoidal curve to simulate the breathing pattern of a volume enlarging process followed by a volume shrinking. The surface points of the sphere are used as the shape surrogate to carry out the

SCDS motion prediction. With the same date set, Gaussian noise is added to create the test data. The Euclidean mean image for the training and test data are shown in Figure 4a and Figure 4a respectively.

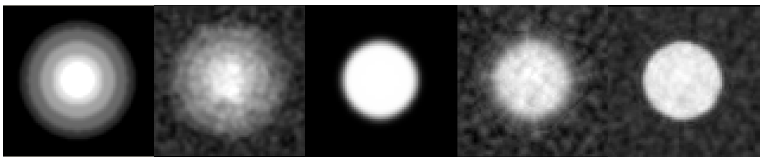

(a) (b) (c) (d) (e)

Fig. 4: Breathing spheres test: a) The Euclidean mean of the original sequence image; b) The Euclidean mean of the noisy test sequence image.CDS motion prediction on noisy breathing spheres; c) The Fréchet mean image of the training data; d)The Fréchet mean image of the test data using the intensity-based atlas formation method; e) The resulting atlas image of the test data using the SCDS motion prediction.

Using the breathing spheres, we first compare the effectiveness of the SCDS motion prediction method (Section 2.2) to the intensity-based atlas method (Section 2.1). The underlying correlation between the surrogate, the surface point set sampling on the spheres with groupwise correspondence, and the image deformation are the same for the training and the testing data, since the only difference between the two datasets is the added Gaussian noise. It is shown that the intensity-based atlas formation method (Figure 4d) tends to over-fit the noise, while the SCDS prediction (Figure 4e) is only determined by the training data.

To simulate the changes or statistical modeling errors in the correlations between the training set and the test set, the correlation coefficients were perturbed randomly by 0.15 at maximum. The results of three methods are shown in Figure 5. The SCDS prediction is influenced by artificial perturbation and produces errors mostly visible at the edge of the atlas sphere. On the other hand, it is shown that the prediction-driven deformation is able to balance between the intensity force and the prediction force thus getting the best result. Errors and intensity energies are shown at each iteration step in Figure 6 for a detailed investigation.

3.2 NCAT data

4D Nurbs-based Cardiac-Torso (NCAT) phantom thorax CTs were produced [16] at 10 phases sampled in one breathing cycle. A corresponding CBCT sequence was simulated from the NCAT CTs using the protocol of a gantry-mounted KV on-board imaging system (Varian Medical Systems) [4] that is used in patient radiation therapy guidance. An example image pair is given in Fig. After a binary segmentation of the lung region, point distribution models (PDMs) were

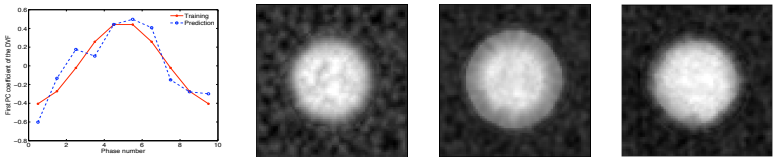

Fig. 5: Test on noisy spheres with slight correlation perturbations (from left to right): 1) The resulting perturbation on the predicted deformations measured in terms of the first principal component coefficients in its training deformation space; 2) The intensity-based atlas image; 3) The atlas image from the SCDS-predicted deformations; 4) The prediction-driven atlas image.

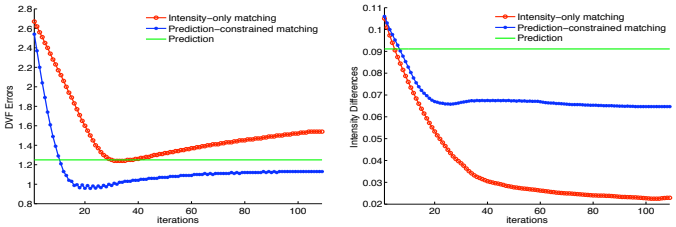

Fig. 6: Comparison results of the deformation estimation on the noisy data. Left: Average displacement vector field error at each iteration, with the ground truth deformations calculated from the training images. Right: Average image intensity force at each iteration. The intensity-based matching method is shown to over-fit the noise.

created using a point-based method that optimizes the group-wise correspondence while sampling on the surface [17]. Meshes were then interpolated from the corresponding surface points, see Figure 7.

In order to test the prediction-driven atlas formation method, variations in the breathing patterns between the training data and the test data were simulated in two experiments. In the first test, we simulate the variation by using different physical parameters for the two NCAT data sets. The parameters that we used for the training set had a maximum of 1.5 cm diaphragm motion and 1.5 cm anterior-posterior motion. The testing data had a maximum of 2.0 cm diaphragm motion and 0.5 cm anterior-posterior motion. All other parameters for the phantom were the same. In the second test, we added random perturbation the correlation coefficients to generate noisy prediction results.

The intensity-based atlas formation results, the SCDS motion prediction results and the prediction-driven atlas formation results are compared in terms of the center of gravity (COG) location errors of the tumor region, shown in Figure 8. The intensity-based atlas method is able to closely capture the tumor location changes. In fact, despite the global streak artifacts, the tumor region after the

CBCT reconstruction still has a quite strong contrast respect to its surrounding tissue. In the real patient CBCT images, less contrast on the tumors is expected.

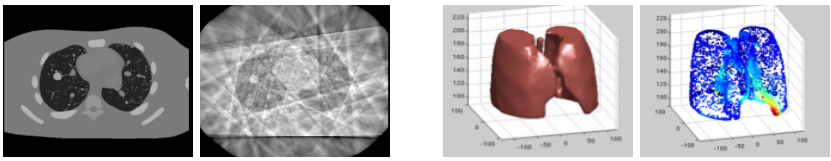

Fig. 7: NCAT simulation: Left) An axial slice of a NCAT CT image at EE phase and its corresponding CBCT image; Right)The surface mesh representation of the shape of lungs extracted from NCAT CTs. The color shows the magnitude of the spatial variation of each point during the breathing cycle.

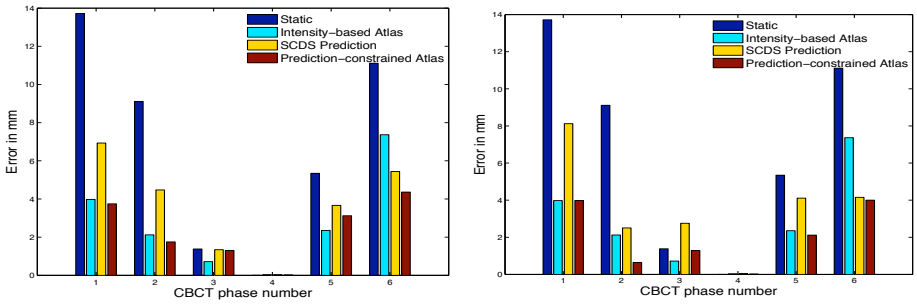

Fig. 8: Three methods are compared in two tests in terms of the tumor COG estimation errors, with the static measurement indicating the mobility of the tumor. The fourth phase is used as the base phase to propagate the tumor contour to other phases. Left: Training and test data sets have different physical motion paramters. The average errors for the four methods in order are 6.79 mm, 2.76 mm, 3.64 mm and 2.38 mm respectively. Right: Test data has correlation pertubations. The average errors for the four methods in order are 6.78 mm , 2.76mm, 3.61mm and 2.0mm respectively.

3.3 Patient data

Respiration-correlated CT (RC-CT) data sets are provided by a 4-slice scanner (lightSpeed GX/i, GE Medical System), acquiring repeat CT images for a complete respiratory cycle at each couch position while recording patient respiration (Real-time Position Management System, Varian Medical Systems). The

CT images are retrospectively sorted (GE Advantage 4D) to produce a series of 3D images at different respiratory time points. The CBCT scans are five-minute scans acquired using a gantry-mounted KV on-board imaging system (Varian Medical Systems).

Motion estimation results are evaluated on a mock tumor region as shown in Figure 9. Manual segmentations are provided for each CBCT image for error measurements. The manual tumor contour of the fourth phase image (the end-expiration phase) is propagated to all the other phases. The three methods are compared in terms of the COG location errors, see Figure 9. The average COG errors of the 5 phases for the three approaches are 3.5 mm, 2.3 mm and 1.7 mm respectively. The prediction-driven atlas method outperforms the other two approaches in this patient.

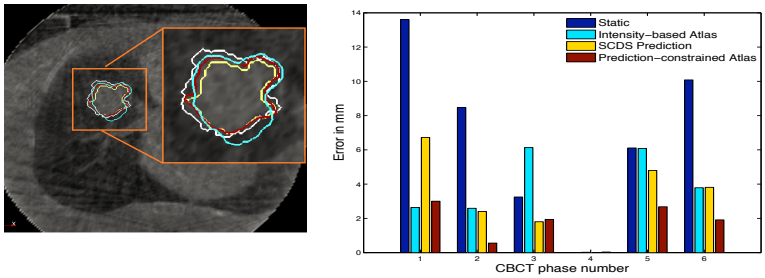

Fig. 9: Three methods are compared in terms of the COG estimation errors, with the static measurement indicating the mobility of the tumor. Left: Axial slices of the estimated tumor contours at the fifth phase from the three methods, with the same colors tagged in the bar figure on the right. The manual segmentation of the tumor contours is shown in white. Right: The COG errors for the four methods. The fourth phase is used as the base phase.

4 Conclusion

The prediction-driven atlas formation framework is shown to be more robust for modeling and estimating sophisticated respiratory motion in lung than the intensity-based Fréchet mean method and the learning-based SCDS motion prediction method, with our preliminary studies on both simulated phantom data and cone-beam CT data. More comprehensive validations on patient data are needed to quantify the robustness of the method.

References

1. Minohara, S., Kanai, T., Endo, M., Noda, K., Kanazawa, M.: Respiratory gated irradiation system for heavy-ion radiotherapy. Int J Radiat Oncol Biol Phys **47**(4) (Jul 2000) 1097–103

2. Keall, P.J., Mageras, G.S., Balter, J.M., Emery, R.S., Forster, K.M., Jiang, S.B., Kapatoes, J.M., Low, D.A., Murphy, M.J., et al.: Task group 76 report on 'the management of respiratory motion in radiation oncology'. Med Phys **33**(12) (Oct 2006) 3874–3900
3. Jaffray, D., Siewerdsen, J., Wong, J., A.A., M.: Flat-panel cone-beam computed tomography for image-guided radiation therapy. Int J Radiat Oncol Biol Phys **53** (2002)
4. Kriminski, S.A., Lovelock, D.M., Seshan, V.E., Ali, I., Munro, P., Amols, H.I., Fuks, Z., Bilsky, M., Yamada, Y.: Comparison of kilovoltage cone-beam computed tomography with megavoltage projection pairs for paraspinal radiosurgery patient alignment and position verification. Int J Radiat Oncol Biol Phys **71**(5) (Aug 2008) 1572–80
5. Zhang, Q., chi Hu, Y., Liu, F., Goodman, K., kenneth E. Rosenzweig, Mageras, G.S.: correction of motion artifacts in cone-beam ct using a patient-specific respiratory motion model. Medical physics **37**(6) (June 2010) 2901–2910
6. Sonke, J., Zijp, L., Remeijer, P., van Herk, M.: Respiratory correlated cone beam CT. Medical Physics **32**(4) (April 2005) 1176–1186
7. Reinhardt, J.M., Christensen, G.E., Hoffman, E.A., Ding, K., Cao, K.: Registration-derived estimates of local lung expansion as surrogates for regional ventilation. Inf Process Med Imaging **20** (2007) 763–74
8. Ehrhardt, J., Werner, R., Schmidt-Richberg, A., Schulz, B., Handels, H.: Generation of a mean motion model of the lung using 4d ct image data. Eurographics Workshop on Visual Computing for Biomedicine (2008) 69–76
9. Gao, G., McClelland, J., Tarte, S., Blackall, J., Hawkes, D.: Modelling the respiratory motion of the internal organs by using canonical correlation analysis and dynamic mri. In: The First International Workshop on Pulmonary Image Analysis, MICCAI 2008, London, UK. (2008) 145–155
10. Dirk, M., Kay, N., Peter, B.: Novel prospective respiratory motion correction approach for free-breathing coronary mr angiography using a patient-adapted affine motion model. Magnetic Resonance in Medicine **50** (2003) 122 – 131
11. Low, D., Parikh, P., Lu, W., Dempsey, J., Wahab, S., Hubenschmidt, H., Nystrom, M., Handoko, M., Bradley, J.: Novel breathing motion model for radiotherapy. International Journal of Radiation Oncology Biology Physics **63** (2005) 921–929
12. Zhang, Q., Pevsner, A., Hertanto, A., Hu, Y., Rosenzweig, K., Ling, C., Mageras, G.: A patient-specific respiratory model of anatomical motion for radiation treatment planning. Medical Physics **34** (2007) 4772–4781
13. Liu, X., Saboo, R., Pizer, S., Mageras, G.: A shape-navigated image deformation model for 4D lung respiratory motion estimation. In: Biomedical Imaging: From Nano to Macro, 2009. ISBI '09. IEEE International Symposium on. (2009) 875–878
14. Liu, X., Oguz, I., Pizer, S.M., ageras, G.S.: Shape-correlated deformation statistics for respiratory motion prediction in 4d lung. SPIE Medical Imaging **Vol. 7625** (Feb 2010)
15. Davis, B.C., Fletcher, P.T., Bullitt, E., Joshi, S.C.: Population shape regression from random design data. In: ICCV, IEEE (2007) 1–7
16. Segars, W.P., Lalush, D.S., Tsui, B.M.W.: Modeling respiratory mechanics in the mcat and spline-based mcat phantom. IEEE Transactions on Nuclear Science **48** (2001) 89–97
17. Oguz, I., Cates, J., Fletcher, T., Whitaker, R., Cool, D., Aylward, S., Styner, M.: Cortical correspondence using entropy-based particle systems and local features. In: Biomedical Imaging: From Nano to Macro, 2008. ISBI 2008. 5th IEEE International Symposium on. (2008) 1637–1640